Schizosaccharomyces pombe kinesin-5 switches direction using a steric blocking mechanism

Mishan Britto[a], Adeline Goulet[b,1,2], Syeda Rizvi[b,1], Ottilie von Loeffelholz[b], Carolyn A. Moores[b], and Robert A. Cross[a,3]

[a]Centre for Mechanochemical Cell Biology, Warwick Medical School, University of Warwick, Coventry CV4 7AL, United Kingdom; and [b]Institute of Structural and Molecular Biology, Birkbeck College, London WC1E 7HX, United Kingdom

Edited by J. Richard McIntosh, University of Colorado, Boulder, CO, and approved October 17, 2016 (received for review July 14, 2016)

Cut7, the sole kinesin-5 in *Schizosaccharomyces pombe*, is essential for mitosis. Like other yeast kinesin-5 motors, Cut7 can reverse its stepping direction, by mechanisms that are currently unclear. Here we show that for full-length Cut7, the key determinant of stepping direction is the degree of motor crowding on the microtubule lattice, with greater crowding converting the motor from minus end-directed to plus end-directed stepping. To explain how high Cut7 occupancy causes this reversal, we postulate a simple proximity sensing mechanism that operates via steric blocking. We propose that the minus end-directed stepping action of Cut7 is selectively inhibited by collisions with neighbors under crowded conditions, whereas its plus end-directed action, being less space-hungry, is not. In support of this idea, we show that the direction of Cut7-driven microtubule sliding can be reversed by crowding it with non-Cut7 proteins. Thus, crowding by either dynein microtubule binding domain or Klp2, a kinesin-14, converts Cut7 from net minus end-directed to net plus end-directed stepping. Biochemical assays confirm that the Cut7 N terminus increases Cut7 occupancy by binding directly to microtubules. Direct observation by cryoEM reveals that this occupancy-enhancing N-terminal domain is partially ordered. Overall, our data point to a steric blocking mechanism for directional reversal through which collisions of Cut7 motor domains with their neighbors inhibit their minus end-directed stepping action, but not their plus end-directed stepping action. Our model can potentially reconcile a number of previous, apparently conflicting, observations and proposals for the reversal mechanism of yeast kinesins-5.

Cut7 | kinesin-5 | bidirectional kinesin | mitotic kinesin | kinesin crowding

Kinesin-5 is essential for mitosis in many eukaryotes, from yeast to humans. Its main function appears to be to establish spindle bipolarity by driving the spindle poles apart during mitotic prophase (1). All kinesins-5 studied to date are homotetramers that crosslink and slide microtubules (MTs), and until recently, all were thought to be plus end-directed (2–8), meaning that their stepping action drives antiparallel MTs to slide slowly apart, with minus ends out. However, it was recently shown that a yeast kinesin-5, *Saccharomyces cerevisae* Cin8, not only can step toward MT plus ends, but also can move rapidly and processively toward MT minus ends (9, 10). The mechanism and biological significance of this bidirectionality are unknown.

Several factors have already been shown to influence kinesin-5 directional switching. Cin8 is a tetramer (11) that steps toward plus ends when linking antiparallel MTs but toward minus ends when moving as a single molecule on un-crosslinked MTs. Crosslinking of two MTs is required for plus end-directed stepping (5), such that the engagement of only one MT turns off plus end-directed motility but supports minus end-directed motility (10, 12). The MT sliding direction of Cin8 also has been shown to reverse according to the surface density of motors in microtubule sliding assays (9), with some dependence on MT length as well, suggesting that the total number of motors interacting with each MT may be the key parameter for directional reversal. A related proposal is that the torsional stress and/or strain developed between crosslinked microtubules might turn kinesin-5 motors on and off (13). This proposal stems from the structure of the antiparallel overlap zone of the *Drosophila* Klp61f tetramer (14), which reveals a rotational offset between the two ends of the tetramer. The stepping direction of Cin8 also depends on ionic strength (12), due in part at least to a Cin8-specific loop L8 sequence (15). Phosphorylation of sites in the Cin8 motor domain also can influence stepping direction (16). Recent evidence also implicates the C-terminal tail of Cin8 (17) in regulating directional reversal. Kip1, the other kinesin-5 in *S. cerevisae*, also has been shown to be bidirectional (18), as has Cut7, the sole kinesin-5 in *Schizosaccharomyces pombe* (19). Cut7 is essential for spindle bipolarity in *S. pombe* (20), and also plays a role in chromosome congression (20).

Given the critical mitotic role of kinesin-5 motors and their corresponding importance as targets for antimitotic agents (21), it is important to understand how they switch direction. We have studied Cut7. We show here that full-length Cut7 can slide MTs bidirectionally in bundles, and that the MT sliding direction in surface assays depends on the local density of Cut7 motor domains engaged with the MT lattice. Our data indicate that Cut7 has a proximity sensor that reverses its direction of progress depending on the local density of motors. To explain this, we propose that steric clashes between neighboring Cut7 motor domains on the MT lattice inhibit their minus end-directed mode, but not their plus end-directed mode. We validate our steric blocking model by demonstrating that the stepping direction of Cut7 can be reversed by crowding it with non-Cut7 lattice binders.

Significance

Molecular motors organize cells by hauling molecular cargoes along polymer tracks (actin filaments or microtubules). Until recently, the stepping direction of each motor was thought to be fixed; however, it now emerges that yeast kinesin-5 motors can reverse their stepping direction. How does this work? We show that the stepping direction of Cut7, a yeast kinesin-5 motor, depends on the level of motor crowding on the microtubule, and that crowding of Cut7 by non-Cut7 proteins also can drive reversal. To explain this, we propose that stepping of Cut7 in one direction is blocked by collisions with neighbors, whereas stepping in the other direction, being less space-hungry, is not. Crowding-dependent directional reversal is a hitherto-unsuspected aspect of motor-driven self-organization in cells.

Author contributions: M.B., A.G., S.R., O.v.L., C.A.M., and R.A.C. designed research; M.B., A.G., S.R., and O.v.L. performed research; M.B., A.G., S.R., O.v.L., C.A.M., and R.A.C. analyzed data; and C.A.M. and R.A.C. wrote the paper.

The authors declare no conflict of interest.

This article is a PNAS Direct Submission.

Freely available online through the PNAS open access option.

Data deposition: The cryo-EM reconstruction reported in this paper has been deposited in the Electron Microscopy Data Bank, https://www.ebi.ac.uk/pdbe/emdb/ (accession no. 3445), and the docked coordinates have been deposited in the Protein Data Bank (PDB), www.pdb.org (PDB ID codes 5M5I and 5M5L–5M5O).

[1]A.G. and S.R. contributed equally to this work.

[2]Present address: Architecture et Fonction des Macromolécules Biologiques, UMR 7257, CNRS, Aix-Marseille Université, 13288 Marseille Cedex 09, France.

[3]To whom correspondence should be addressed. Email: r.a.cross@warwick.ac.uk.

This article contains supporting information online at www.pnas.org/lookup/suppl/doi:10.1073/pnas.1611581113/-/DCSupplemental.

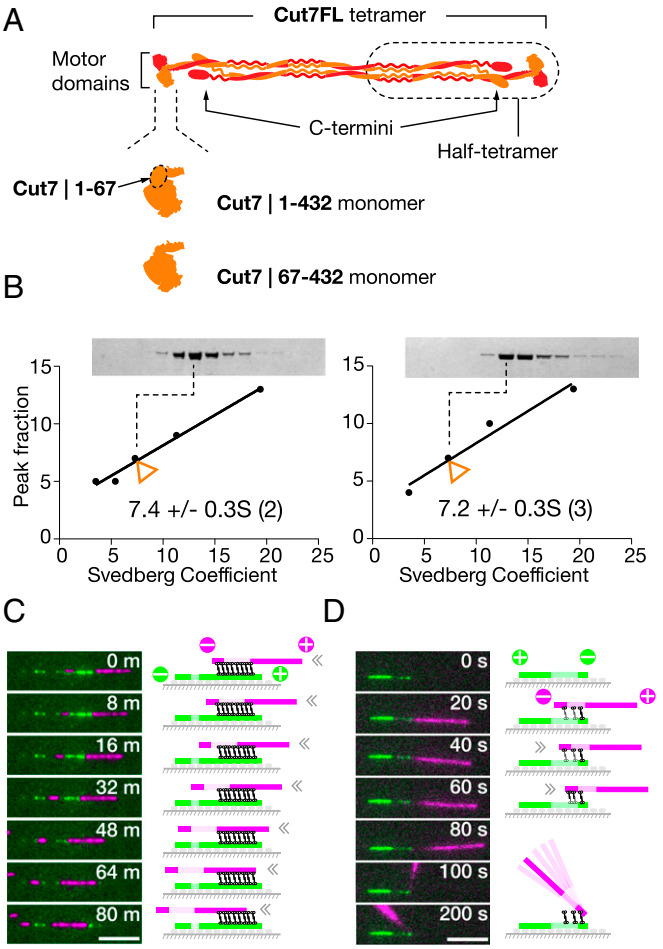

Fig. 1. (*A* and *B*) Cut7FL (*A*) was subjected to glycerol gradient centrifugation (*B*) in (*Left*) KPEM100 buffer (100 mM PIPES, 1 mM EGTA, 1 mM $MgSO_4$, pH 6.9) + 300 mM NaCl and (*Right*) KPEM100 only to determine its S-value. (*C* and *D*) Cut7-driven gliding of (magenta) polarity-marked cargo MTs on (green) polarity-marked rail MTs in KPEM100 + 100 mM NaCl, 4 mM MgATP. (*C*) Magenta cargo MTs slide slowly from right to left along green rail MTs, indicating plus end-directed motor activity. Note that the MTs are parallel, implying that one end of the Cut7 tetramer is moving faster than the other. (*D*) Magenta cargo MTs slide rapidly from left to right with the plus end leading. MTs are antiparallel, so sliding must be driven by minus end-directed force. At the end of its travel, the cargo MT pivots for several seconds with its tip attached to the tip of the rail MT. (Scale bars: 5 μm.) Refer to Movies S2–S4. The motor locations in the cartoons are speculative.

Results and Discussion

Cut7FL Moves Microtubules Bidirectionally in Bundles. We chose to work with tetrameric Cut7FL because there is evidence that in Eg5, a mammalian kinesin-5, the C termini of each constituent dimer lie close to the motor domains of its partner (Fig. 1*A*), and potentially can contribute to function. It was recently shown that deleting the C-terminal tail of Cin8 abrogates MT crosslinking (17). For our microtubule sliding experiments, we used polarity-marked MTs, assembled by polymerizing fluorescent tubulin onto short, stabilized MT seeds that were labeled more brightly or in a different color (*Methods*). Initial experiments in solution established that Cut7FL bundles and parallelizes microtubules (Movie S1). In subsequent experiments, we assembled Cut7FL crosslinked bundles in solution using two classes of polarity-marked MTs, labeled in different colors, one with biotinated tubulin and one without. Bundles consisting of only two MTs were selected, and the sliding of the upper MT relative to the immobile surface-tethered MT was recorded. These experiments show that tetrameric Cut7FL (Fig. 1*B*) can drive MTs in bundles to slide in either direction (Fig. 1 *C* and *D* and Movies S2–S4).

The Direction of Cut7FL-Driven MT Gliding Depends on the Concentration of Lattice-Engaged Motors. To try to understand what sets the direction of Cut7-driven MT motility, both in MT bundles and potentially elsewhere, we performed in vitro MT gliding assays, using antibodies to link Cut7FL motors to glass coverslips via their C-terminal 6-his tags. Because in our assays Cut7FL tetramers were tethered to the surface, we were effectively testing half-tetramer–driven MT gliding (Fig. 1*A*). In these assays, MT velocity and direction depend on both the density of Cut7FL motors on the coverslip and the ionic strength, as reported previously for Cin8 and other yeast kinesins-5. At low ionic strength in KPEM gliding buffer (Fig. 2*A*), sparse Cut7FL surfaces drive MTs to slide rapidly with their plus ends leading, indicating that the surface-attached Cut7FL motors are stepping toward MT minus ends (Movie S5). On very sparse Cut7FL surfaces, MTs pivot about single points on the surface as they slide (Movie S6), suggesting a minimal processive unit at each locus, presumably a single half-tetramer. Increasing the density of Cut7FL on the coverslip surface under these conditions decreases the MT sliding velocity, and at the highest densities the sliding direction reverses (Fig. 2*A*), so that dense Cut7FL surfaces under these conditions drive only plus end-directed sliding (Movie S7). By serially changing the buffer composition, dense Cut7FL surfaces can be switched from net minus end-directed to net plus end-directed force generation and back again (Fig. 2*C* and Movie S8).

Previous work has shown that the directionality of Cin8 depends on motor surface density, MT length (9), and ionic strength (22). Based on the MT length dependence of directional switching, it has been proposed that the important parameter for directional switching is the total number of motors engaged by a particular MT (9). For Cut7, we found that if we neglect the intervals during which the sliding MTs pause, then the velocity distributions for Cut7-driven sliding of short (<7.5 μM) and long (>7.5 μM) MTs are indistinguishable (Fig. 2*C*). Thus, our Cut7 data suggest that the key determinant of directionality is the level of crowding of Cut7 motor domains on the MT lattice. The ionic strength dependence of MT sliding direction is consistent with this idea, because ionic strength will influence the lattice occupancy of kinesin motor domains (23), but not their density on the coverslip. Overall, our results strongly suggest that the stepping direction of Cut7 motor domains is determined by their lattice density, indicating a proximity sensing mechanism.

Monomeric Cut7 Motor Domains Generate Only Plus End-Directed Sliding Force. To further investigate the basis for Cut7 directional reversal, we engineered monomeric (single motor domain) Cut7 constructs with and without the Cut7-specific ~65 residue N-terminal extension domain (Fig. 1*A*). Both constructs also contained a C-terminal 6-his tag. N-terminally truncated Cut7|67–432 monomers linked via his tag antibodies to coverslips drive consistent plus end-directed MT sliding at ~10 nm s^{-1}, independent of MT length (Fig. 2*D* and Movie S9). However, this N-terminally truncated construct requires low ionic strength (30 mM PIPES) to function effectively; at higher ionic strengths, MTs dissociate. Cut7|1–432 monomers with an intact N-terminal extension also drive robust, plus end-directed MT sliding (Fig. 2*E* and Movie S10). These data show that monomeric Cut7 motor domains generate only plus end-directed steps, implying that minus end-directed stepping by Cut7 requires linked pairs of motor domains, as in the intact half-tetramer. Our data also show that the Cut7-specific N-terminal extension domain is not required for plus end-directed stepping. Our data are complementary to recent work by Edamatsu (19), who showed that deletion of the Cut7 N terminus does not abrogate in vivo function, but does affect MT affinity in vitro.

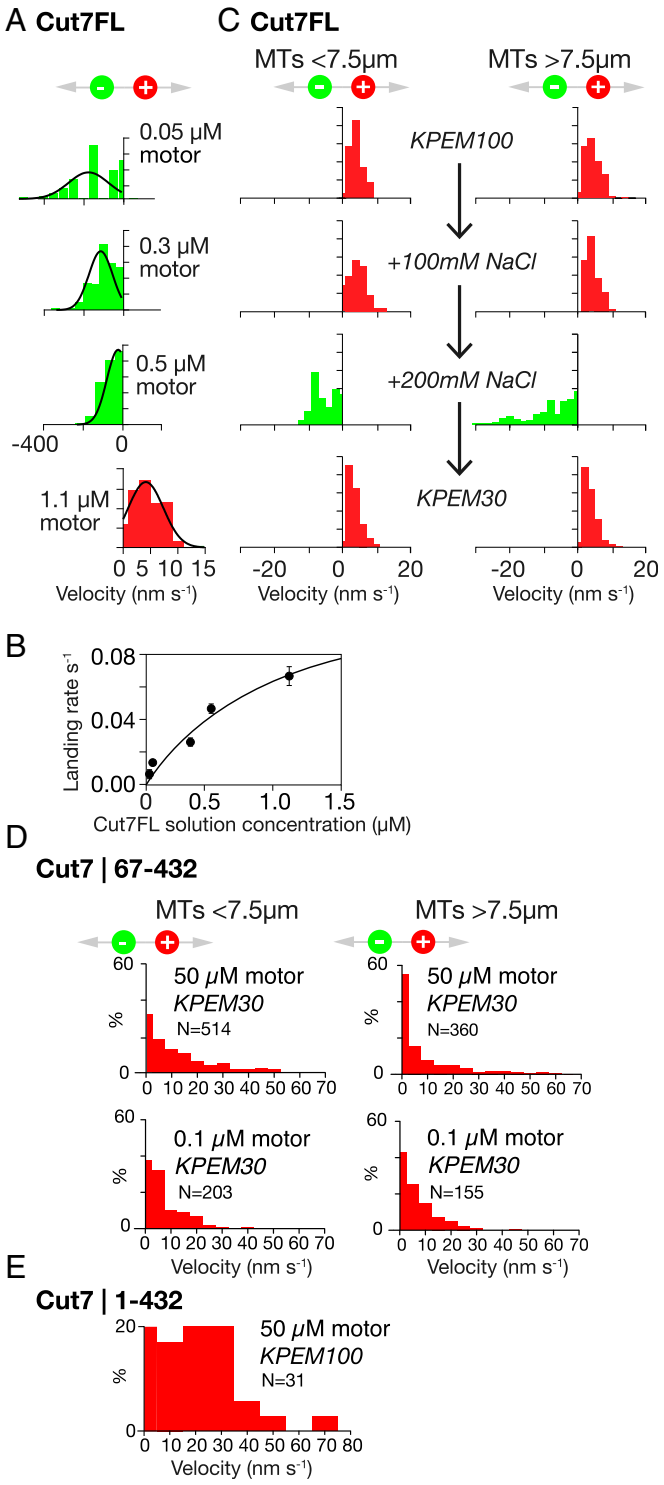

Fig. 2. In vitro motility. (*A*) Directional reversal by increasing the surface density of Cut7FL. Increasing motor density slows MT sliding and ultimately drives directional reversal. Note the expanded velocity axis for plus end-directed stepping. The concentrations shown are the solution concentrations of Cut7FL used to prepare the surfaces. (*B*) Control experiment showing that this concentration scales predictably with the MT landing rate, which in turn is proportional to the surface density of active motor. (*C*) Lawns of Cut7FL motors can be converted back and forth between plus and minus end-directed stepping by serially changing the ionic strength. All data are from the same flow cell with a dense surface of Cut7FL. The initial buffer was KPEM100 gliding buffer, 1 mM ATP (*Methods*), followed by the same plus 100 mM NaCl, and then the same plus 200 mM NaCl (note the directional reversal). Finally, flushing with KPEM30 gliding buffer, 1 mM ATP reverted the motor to plus end-directed stepping. Data from short (<7.5 μm) and long (>7.5 μm) MTs are very similar. An MT length of 7.5 μm was chosen to split the data approximately in half (Movie S8). (*D*) In 30 mM PIPES pH 6.9 and 0.1 mM ATP, Cut7|67–432 monomers drive MTs to slide with plus ends trailing, independent of MT length and motor density. (Movie S9). (*E*) Cut7|1–432 monomers also drive MTs to slide with plus ends trailing (buffer, 100 mM PIPES pH 6.9 and 0.1 mM MgATP) (Movie S10).

The Extended N-Terminal Domain of Cut7 Increases MT Affinity but Also Adds Drag. To check for an influence of the Cut7 N terminus on MT affinity, we expressed the Cut7 N-terminal extension as a GFP fusion protein, and performed spin-down assays with MTs (see also ref. 24). GFP alone did not pellet with MTs, but GFP fused to the Cut7 N terminus did (Fig. 3*A*), confirming that the Cut7 N terminus binds directly to MTs. As a further check, we fused the Cut7 N-terminal domain to the N terminus of kinesin-1. Ordinarily, MT sliding velocity for wild type kinesin-1 is independent of ionic strength; however, with the Cut7 N terminus attached, MT sliding velocity decreased at low ionic strength (Fig. 3*B*), indicating that the Cut7 N-terminal extension enhances MT binding, but at the expense of increased drag.

Structure of the Cut7 Monomer in the MT-Bound AMPPNP State. Given that our motility assay data indicated a key role for Cut7 occupancy on the MT lattice in determining directionality, we felt it important to visualize the lattice-attached strong-state Cut7 motor domain. We used cryoEM to visualize the motor domain in a force-generating conformation. We calculated a 9.3-Å resolution reconstruction (Fig. S1) of Cut7|1–432 bound to MTs in the presence of AMPPNP, a nonhydrolyzable ATP analog, and identified individual secondary structural elements within the motor domain.

Our analysis (Fig. 4 and Movie S11) demonstrates that the overall conformation of the Cut7-AMPPNP bound to MTs is very similar to that of the equivalent human kinesin-5 reconstruction (25), consistent with a canonical plus end-directed power stroke. Specifically, (*i*) the major contacts between the motor and the MT are formed by the relay helix α4 (25, 26); (*ii*) with AMPPNP bound, the highly conserved nucleotide sensing loops switch I and switch II adopt a closed configuration around the nucleotide (25, 26); and (*iii*) as a consequence, density corresponding to the Cut7 neck linker (red) is in a so-called "docked" configuration directed toward the MT plus end. However, several distinctive features of the Cut7 sequence compared with human kinesin-5 are also apparent, for example, an elongated loop L10 at the plus end of the motor (orange) and a shorter and less distinctively curled loop L5 (pink) (25, 26). In addition, partial density corresponding to the Cut7-specific N-terminal extension is visible in our reconstruction (dark blue/cyan) emerging from the motor domain proximal to the neck linker; however, the N terminus was so mobile in our reconstructions that we could model it only partially. Indicative locations for its most proximal 10 amino acids are shown in Fig. 4 and Movie S11. Only one of these locations (in dark blue) would allow formation of a cover neck bundle, the structure by which the neck linker and N terminus of plus end-directed motors are thought to collaborate to generate plus end-directed force (25–27). Thus, our cryoEM 3D reconstruction of MTs bound by Cut7 establishes that Cut7 is like other kinesin-5 family members in the majority of its structural features, while also containing regions of structural divergence specific to Cut7. In particular, the connection between L10 and the distal part of the neck linker densities in our reconstruction indicates that L10 could play a role in regulating neck linker docking.

Overall, our determined structure for Cut7 monomers bound to MTs in AMPPNP closely resembles that of the corresponding Eg5 complex, consistent with an Eg5-like plus end-directed conformational cycle in which in AMPPNP, the neck linker anneals into its docking station on the head. Part of the unusual extended N terminus

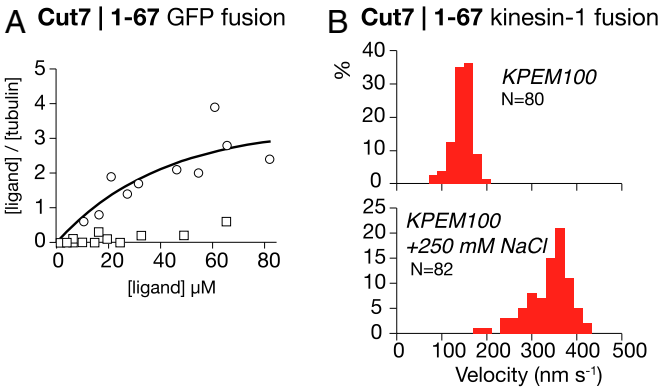

Fig. 3. (*A*) Spin-down assay showing that Cut7 N-terminal domain C-terminally fused to GFP (circles) binds to MTs, whereas GFP alone (open squares) does not. The buffer comprised 25 mM PIPES pH 6.8, 30 mM NaCl, 7 mM $MgCl_2$, 1 mM EGTA, and 1 mM 2-mercaptoethanol. (*B*) MT sliding driven by kinesin-1 dimers fused to the Cut7 N terminus. MTs move slowly (*Upper*) in KPEM100 gliding buffer, and faster (*Lower*) in KPEM100 + 250 mM NaCl gliding buffer, 1 mM ATP.

of Cut7 lies alongside the main part of the head, close to the docked neck linker, whereas the remainder appears mobile. Thus, the N-terminal extension of Cut7 could serve to increase the space occupied by the motor domain and to boost its MT affinity, although in the context of the saturated MT lattice of our cryoEM sample, direct contact of the N terminus with the MT surface is not evident.

Crowding of Cut7FL with Non-Cut7 Proteins Reverses the MT Gliding Direction. Our finding that directional switching of Cut7 is correlated with lattice crowding suggests that lattice-attached Cut7 motor domains have a proximity-sensing mechanism. To account for this, we propose a steric blocking model, in which steric clashes between lattice-engaged motors inhibit minus end-directed stepping but not plus end-directed stepping, which we envisage to be less space-hungry. Potentially, the more space-hungry, minus end-directed mode of Cut7FL might correspond to processive walking, as suggested by MT pivoting in sparse motility assays (Movie S6). Our steric blocking hypothesis strongly predicts that crowding of Cut7 by a non-Cut7 competitor should also reverse its stepping direction.

To test this prediction, we first used dynein microtubule binding domain (MTBD) (28) as a crowding agent. Adding this non-Cut7 protein to a moderately dense Cut7FL surface reverses the direction of Cut7-driven MT gliding, so that without MTBD, MTs slide with their plus ends leading (Fig. 5*A*), and with MTBD, they slide with their plus ends trailing (Fig. 5*B* and Movie S12). Increasing the ionic strength reverses the sliding direction (Fig. S2). This confirms that a non-Cut7 competitor can obstruct Cut7 and reverse its stepping direction. To test whether a non-Cut7 kinesin can do the same, we used Klp2, a kinesin-14. We found that MTs glide across Klp2 surfaces with their plus ends leading (Fig. 5*D* and Movie S13), independent of Klp2 density. Nonetheless, adding Klp2 to a suitably dense Cut7FL surface did reverse the MT sliding direction (Fig. 5*E* and Movie S13), showing that indeed Klp2 can crowd Cut7 and convert it from minus to plus end-directed stepping, despite itself stepping toward minus ends. Taken together, the foregoing data confirm that not only CutFL, but also non-Cut7 competitors, can crowd Cut7FL and switch its stepping direction from minus to plus, consistent with our steric blocking hypothesis.

Our proposed steric blocking model for directional reversal offers a framework within which previous, apparently conflicting, proposals for the basis of kinesin-5 bidirectionality might be reconciled. Thus, the reported buffer dependence of Cin8 directional switching (15) (which we also find for Cut7) potentially may be due to lower ionic strength favoring increased occupancy of the MT lattice. The dependence of Cin8 directional switching on the sequence of loop 8 (15) and on phosphorylation of the motor domain (16) might have a similar explanation. The N-terminal extension of Cut7 enhances the MT affinity of the motor domain and thus will increase occupancy. Hackney et al. (24) previously reported that the extended N terminus of BimC also enhances MT binding. For Cin8, it was previously shown that varying the density of motors on the coverslip surface in motility assays can reverse the direction of MT sliding, leading to the proposal that motor–motor coupling was occurring (9). Our findings suggest a specific mechanism for motor–motor coupling, namely mutual steric interference. It also has been proposed that the crosslinking of two MTs by Cin8 tetramers switches Cin8 from minus end-directed to plus end-directed motility (22). For Cut7, we can rule out this possibility, because we see bidirectional sliding of MTs crosslinked by Cut7; however, it is likely that conditions favoring MT crosslinking would also favor lattice crowding, which in our model would in turn favor directional switching. In recent work, Düselder et al. (17) showed

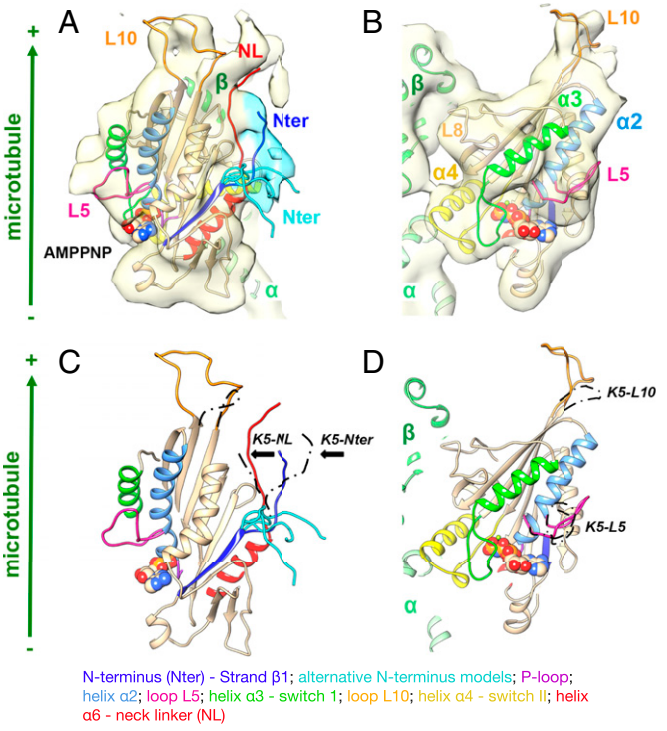

Fig. 4. Structural analysis of MT-bound Cut7 heads. Shown is the 9-Å cryoEM reconstruction and pseudoatomic model of the MT-bound Cut7-AMPPNP motor domain. (*A* and *B*) CryoEM reconstruction, shown as a pale-yellow surface, with density corresponding to the proximal region of the N terminus shaded in cyan. With AMPPNP bound, the Cut7 neck linker (red) is docked toward the MT plus end, whereas density corresponding to the extended N terminus could contribute to formation of a cover-neck bundle (Nter; in blue), but the majority is flexible; exemplar alternative conformations are shown in cyan. (*B*) View toward the nucleotide-binding site. The kinesin-5 specific L5 (pink) protrudes from the surface of the motor, and the density corresponding to the Cut7-specific elongated L10 (orange) at the plus end of the motor is clearly defined and close to the docked neck linker. (*C* and *D*) Comparison of the Cut7-AMPPNP model (rainbow) and human kinesin-5–AMPPNP (K5; position of key loops indicated in dashed black), superimposed on helix-H4. Cut7-L5 (pink) adopts a distinct conformation compared with K5-L5, whereas Cut7-L10 is 17 residues longer compared with K5-L10. The MT plus end is toward the top of this figure (Movie S11).

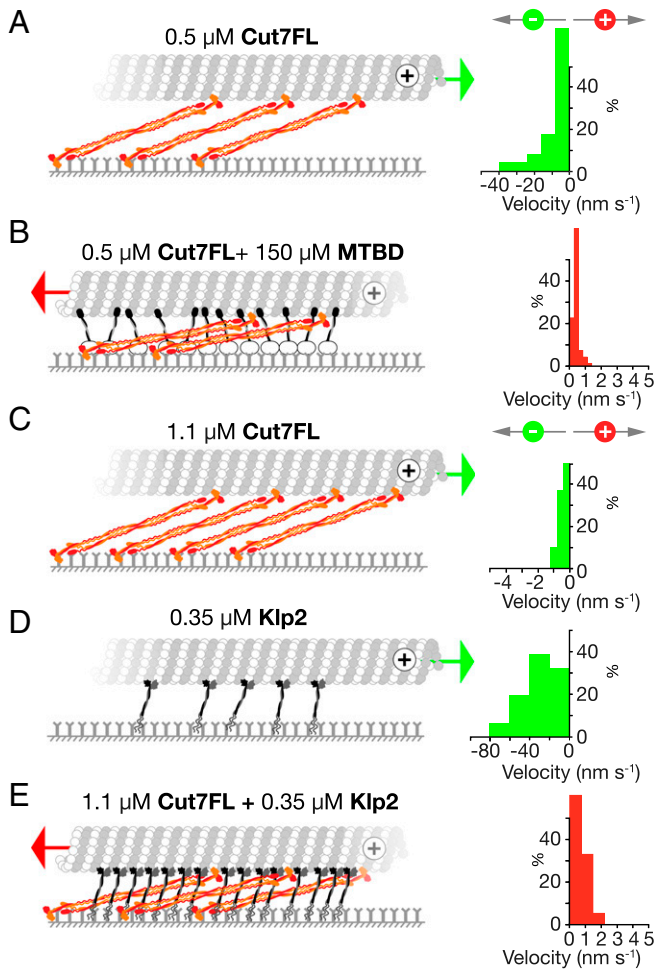

Fig. 5. Non-Cut7 competitors can drive directional reversal of Cut7. (*A*) A 0.5 μM Cut7FL surface. MTs slide with their plus ends leading. (*B*) Same as in *A* plus MTBD. MTs slide with their plus ends trailing. (*C*) A 1.1 μM Cut7FL surface. MTs slide with their plus ends leading. (*D*) A 0.35 μM Klp2 surface. MTs slide with their plus ends leading. (*E*) A Cut7FL + Klp2 surface. MTs slide with their plus ends trailing. Conditions: (*A* and *B*) KPEM100 gliding buffer, 1 mM ATP; (*C*–*E*) same + 150 mM NaCl. The given motor concentrations are the solution concentrations used to make the surfaces (Figs. S2 and S3 and Movies S12 and S13).

that the Cin8 tail domain is required to regulate its directional switching, because a chimeric Cin8 dimer with a kinesin-1 tail is bidirectional but in an unregulated way. Again our proposed steric blocking model is consistent, in that directionality is regulated by an emergent property, steric interference between neighbors. The earlier data of Edamatsu (19) on the effect of truncation on the directionality of Cut7 are consistent as well.

Our finding that the directional reversal of Cut7 depends on steric clashes with neighbors adds a surprising dimension to recent work on the role of "traffic jams" on MTs in the feedback control of molecular motor activity (29), by revealing that the microtubule sliding direction of a mixed population of kinesins can potentially reverse, depending on the pattern and extent of mutual steric interference. Recent optical trapping measurements have shown that for Eg5, which generates plus end-directed sliding force and braking force, the forces scale according to the number of engaged motors, demonstrating that each motor has no effect on the forces produced by its neighbors (30). Our work shows that for Cut7, the opposite is true. The action of each motor is strongly dependent on the proximity of its neighbors, and sliding force will scale in a complicated way, with both the magnitude and the direction of the force critically dependent on the proximity of neighboring motors, and potentially on that of nonmotor microtubule binding proteins as well.

Methods

Constructs and Proteins. Cut7FL (1,085 aa) was PCR-amplified from *S. pombe* genomic DNA and cloned into pET17b between NdeI and SacI sites incorporating a C-terminal His6 tag and N-terminal GST tag, cleavable by PreScission protease. Cut7FL cDNA in pET17b was digested with NotI-HF and NdeI (New England Biolabs), and the insert was subcloned into PGEX 6P-2, modified by inserting a unique Nde I site immediately following the PreScission site using the Quickchange lightning system (Agilent). Expressed Cut7 proteins were purified initially via their His6 tag as described previously (31). The resulting fraction was loaded on to an equilibrated 1-mL GSTrap-HP Column (GE Healthcare) and washed extensively with KPEM100 + 100 mM NaCl, 1 mM ATP, and 10 mM β-mercaptoethanol. Then 100 U PreScission protease (GE Healthcare) in 1.2 mL of column buffer was run into the column, which was then capped and rotated overnight at 4 °C. On the next day, groups of eluted fractions were desalted using Zeba columns (Pierce) into either KPEM100 or KPEM100 + 100 mM NaCl, 10 mM β-mercaptoethanol, and 1 mM ATP. KPEM100 contained 100 mM PIPES, 1 mM $MgSO_4$, and 2 mM EGTA adjusted to pH 6.8 with KOH. For glycerol gradients, the protein was eluted from the GSTrap-HP column at high concentration using a pulse of 50 mM NaCl, 1 mM ATP, 10 mM β-mercaptoethanol, 2 mM $MgCl_2$, 20 mM glutathione, and 20 mM Tris HCl pH 8.0 and digested with 100 U of PreScission protease in a final volume of 1.2 mL This digest was loaded directly onto glycerol gradients (31). Then 260-μL fractions were harvested using a 1-mL Gilson Microman positive displacement pipette. For high salt glycerol gradients, the foregoing buffer was supplemented with 400 mM NaCl. Protein concentrations were estimated using SYPRO red staining (Life Technologies).

For Cut7 monomeric constructs, residues 1–432 of Cut7 (Cut7|1–432) were PCR-amplified from *S. pombe* genomic DNA and cloned into a pET151D-TOPO vector (Invitrogen), adding a TEV protease-cleavable N-terminal His6-tag. The recombinant His6-tagged protein was expressed in BL21*(DE3) *Escherichia coli* cells in LB medium, supplemented with 2% (wt/vol) glucose on induction with 0.5 mM isopropyl β-D-1-thiogalactopyranoside (IPTG) at 18 °C for 5 h. Cells were resuspended in lysis buffer [50 mM Tris·HCl pH 8.0, 400 mM NaCl, 1 mM $MgCl_2$, 1 mM ATP, 5 mM 2-mercaptoethanol, 10% (vol/vol) glycerol, 0.2 mg/mL lysozyme, 0.1 mg/mL DNase I, and EDTA-free Protease Inhibitor Mixture (Roche)] and lysed by sonication. Tagged Cut7-MD was purified from the clarified cell supernatant using nickel affinity. The His6-tag was removed using TEV protease and Cut7-MD was exchanged into 25 mM PIPES pH 6.8, 30 mM NaCl, 7 mM $MgCl_2$, 1 mM EGTA, and 1 mM 2-mercaptoethanol before use in the cryoEM experiments.

For Cut7 monomer gliding assays, an additional monomeric construct, residues 67–432 of Cut7 (Cut7|67–432), was cloned into a pET151D-TOPO vector introducing a second, noncleavable C-terminal His6-tag using site-directed ligation-independent mutagenesis (32). This recombinant, doubly His6-tagged protein was expressed in BL21*(DE3) *E. coli* cells in LB medium, supplemented with 1% glucose on induction with 0.1 mM IPTG at 25 °C for 6 h. Cell pellets were resuspended in lysis buffer (as above), and doubly tagged Cut7|67–432 was purified from the clarified lysis supernatant using nickel affinity chromatography. The N-terminal His6-tag was removed by cleavage with GST-tagged TEV protease (Sigma-Aldrich), and the cleaved protein was separated from the TEV protease using glutathione agarose chromatography. A further doubly His6-tagged Cut7|1–432 construct was cloned in a similar way, but to generate proteolysis-protected Cut7|1–432, an additional StrepII tag was inserted immediately before its N terminus after the TEV cleavage site. This Cut7|1–432 construct was purified using nickel affinity chromatography, followed by TEV cleavage of the N-terminal his-tag and a second purification step using streptavidin beads. The protein was eluted using 5 mM desthiobiotin in the purification buffer (50 mM Tris pH 8, 400 mM NaCl, 1 mM $MgCl_2$, 5 mM 2-mercaptoethanol, and 1 mM ATP) and concentrated for further use. Residues 1–66 of Cut7 (Cut7|1–66) were C-terminally fused with EGFP (followed by a stop codon) by introduction of in-frame BamHI and EcoRI sites in the Cut7|1–432 pET151D-TOPO vector. This fusion protein was expressed and purified as for Cut7|1–432. EGFP alone was also cloned into pET151D-TOPO vector, expressed and purified in the same way, and used as a negative control in the MT binding assay. The N-terminal segment of Cut7 was fused to full-length *Drosophila* kinesin-1 using a Gibson Assembly Cloning Kit (New England Biolabs), and the same vector used to host Cut7FL. The expressed protein was purified and processed as for Cut7FL. Klp2 (33) and dynein p111 MTBD fusion (28) proteins were expressed and purified as described previously.

Polarity-Marked Biotinylated MTs. GMPCPP seed assembly mix used unlabeled stock tubulin supplemented with either 7% (wt/wt) (Hylite 488 TL488M/TL670M/TL590M) tubulin or 10% (wt/wt) biotinylated tubulin (T333; Cytoskeleton) as needed. In protocols using dim seeds, the mix contained 1% label. Seed assembly mix was prepared by mixing stock tubulin into KPEM100 buffer, 10 mM β-mercaptoethanol, and 1mM GMPCPP to 20 μM tubulin concentration, incubating on ice for 30 min, clarifying at 90,000 × *g* for 5 min, and snap-freezing the supernatant in 2.5-μL aliquots in liquid nitrogen. For assembling seeds, the thawed seed mix was diluted to 5 μM tubulin in assembly buffer and then incubated at 37 °C for 30–45 min in a total volume of 10 μL. The elongation mix was prepared identically to the seed mix, except that the tubulin was differently fluorescently labeled and stored in 20-μL aliquots. To elongate seeds, the elongation mix was diluted to 1 μM tubulin, prewarmed at 37 °C, and then added to 10 μL of seeds in a final volume of 200 μL. Elongation was continued at 37 °C for 1.5–2 h. The resulting polarity-marked polymerized MTs were diluted to 0.6 μM (to minimize end-to-end annealing) and held at room temperature. MTs were pelleted in an Airfuge ultracentrifuge (Beckman Coulter) for 5 min, resuspended in gliding buffer (for gliding assay) or KPEM100/200/300 (for studying MT bundling) with 20 μM paclitaxel at a 0.6 μM or 1.2 μM final tubulin heterodimer concentration, and used within 1 h.

MT Gliding Assays. Slides (L4244) and coverslips (L4095-2) (Menzel-Glaser; Agar Scientific) were soaked in 10 M NaOH for 30 min with shaking, transferred to staining racks, rinsed extensively in Millipore water until pH 7.0 was attained, then transferred to 0.25% Neutricon and soaked for 20 min at 75 °C with intermittent sonication, followed by 20 min in Millipore water, again with intermittent sonication. This cycle was repeated twice, followed by extensive washing with Millipore water. Slides and coverslips were stored in Millipore water at 4 °C and used within 3 d, with drying using a Spin Clean (Technical Video) before use. Flow cells were made from coverslips adhered to slides using two parallel strips of double-stick tape and sealed using silicone grease (Beckman Coulter). The gliding buffer was 0/100/200/300 mM NaCl, 10 mM β-mercaptoethanol, 10 mg/mL BSA, 20 μM paclitaxel, 1 mM GMP-CPP, 4/1/0.1 mM Mg-ATP, and oxygen scavenger (20 mM glucose, 0.2 mg/mL catalase, and 0.4 mg/mL glucose oxidase) in KPEM100. Gliding buffer was stored at −80 °C, and aliquots were freshly thawed for each flow cell. Flow cells were rinsed with 5 volumes of primary mouse anti-hexa histidine antibody (MA1-21315; Thermo Fisher Scientific) at 1 mg/mL, incubated for 10 min, and flushed and blocked with gliding buffer. Alternatively, antibody was added at 0.1 mg/mL, and only 1 flow cell volume was introduced to create a lower-density antibody surface. Kinesin solutions were introduced and incubated for 5 min, then flushed with gliding buffer or KPEM100/30/15. MTs in gliding buffer were then introduced at 0.6 μM or 1.2 μM final tubulin heterodimer concentration.

MT Sliding in Bundles. Flow cells were coated with 5FCV neutravidin (5 mg/mL) by incubation for 10 min, then rinsed and blocked with gliding buffer for 10 min. Then 0.6 μM polarity-marked biotinylated MTs (2.5 μL) were mixed with 0.6 μM polarity-marked nonbiotinylated MTs (7.5 μL) and 1.1 μM Cut7FL and immediately injected into the flow cell. After a 10-min incubation, the flow cell was flushed with 5 volumes of gliding buffer in KPEM100 + 100 mM NaCl.

Glycerol Gradients. Glycerol gradient centrifugation was done as described previously (33).

TIRF Microscopy and Analysis. Images were acquired at 25 °C with a humidified environmental stage top incubator (Okolab) on an Olympus CELLR/TIRF microscope using a Hamamatsu ImageEM EMCCD camera with a 100× NA 1.49 objective with or without 1.6× auxiliary magnification, yielding 160 nm or 100 nm pixels in a 512 × 512 field. Polarity-marked MTs were visualized using 488-nm and 561/640-nm laser lines. MT gliding velocity was measured using RETRAC (31) and Metamorph.

MT Spin-Down Assays. Cut7|1–66-eGFP and the eGFP control protein were buffer-exchanged into 25 mM PIPES pH 6.8, 30 mM NaCl, 7 mM $MgCl_2$, 1 mM EGTA, 1 mM 2-mercaptoethanol, and a range of concentrations of each protein titrated against a constant concentration of paclitaxel (Calbiochem)-stabilized bovine brain tubulin MTs (Cytoskeleton). Following incubation at room temperature, the mixture was centrifuged at 392,000 × *g* for 10 min in a Beckman benchtop ultracentrifuge and supernatant, and pellet fractions were analyzed by SDS/PAGE. Protein bands were visualized using SYPRO-Red (Invitrogen) and a Fuji FLA3000 scanner.

EM, Image Analysis, and Atomic Model Building. MTs were polymerized from bovine brain tubulin (Cytoskeleton), at a final concentration of 5 mg/mL at 37 °C for 1.5 h in a buffer containing 100 mM MES pH 6.5, 1 mM $MgCl_2$, 1 mM EGTA, 1 mM DTT, and 2 mM GTP. MTs were stabilized with 1 mM paclitaxel in dimethyl sulfoxide for another 1.5 h at 37 °C. Cut7|1–432 was incubated with 5 mM AMPPNP for 45 min on ice and mixed with a 10-fold molar excess of MTs (2 μM) for 5 min at room temperature. Subsequently, 3.5 μL was applied to glow-discharged C-flat holey carbon grids (Protochips) at 24 °C and 100% humidity, and then blotted and plunged into liquid ethane (Vitrobot; FEI). Low-dose micrographs were recorded with a Tecnai F20 FEG microscope (FEI) operated at 200 kV, 0.7–2.6 μm defocus, and 68,000× magnification on a Gatan Ultrascan 4000 CCD camera with sampling of 2.2 Å/pixel.

The 3D reconstruction was calculated using a previously described custom single particle procedure (32, 34). A total of 144,300 asymmetric units (Cut7 motor domain bound to an αβ-tubulin dimer) were boxed along 233 13-protofilament MTs using BOXER (35), and the seam orientation was determined by projection matching using custom SPIDER scripts (36) and refined with FREALIGN (37). The final reconstruction was calculated using particles with an isotropic angular distribution and by taking into account pseudo-helical symmetry using FREALIGN (37). The resolution was estimated at 9.3 Å using the Fourier shell correlation 0.5 criterion.

An initial homology model of the AMPPNP-bound Cut7 motor (residues 70–432) based on human K5-AMPPNP–bound structure [Protein Data Bank (PDB) ID code 3HQD] was prepared using Modeler. The coordinates of the Cut7 motor domain bound to an αβ-tubulin dimer (PDB ID code 1JFF) were rigidly fitted into the cryoEM map using UCSF Chimera (38) and refined by flexible fitting using Flex-EM (39). Structural models of loop 5 and loop 10, which are shorter and longer, respectively, than in human K5, were generated using Modeler and selected on the basis of the highest cross-correlation value. The conformation of the neck linker and the N terminus were calculated using a conjugate-gradient energy minimization approach implemented in Flex-EM and selected according to the same criterion. Five clusters of N terminus conformations were produced by ranking nine models based on the CC value and an rmsd clustering Cα cutoff of 1 Å. The final Cut7 motor domain model was energetically minimized, and its stereochemistry was checked.

ACKNOWLEDGMENTS. We thank Charles Sindelar (Yale University) for reconstruction algorithms, Andrew Carter (Medical Research Council Laboratory for Molecular Biology) for the dynein MTBD fusion construct, and Douglas Drummond and Gillian Fox (both at Warwick Medical School) for the initial Cut7 construct in pET17b. We also thank Naomi Sheppard (Warwick Medical School) for expressing and purifying the dynein fusion protein. Funding for this work was provided by Biotechnology and Biological Sciences Research Council Grant BB/H005137/1 (to C.A.M., A.G., and S.R.) and Worldwide Cancer Research Grant 11-0261 (to C.A.M., A.G., and S.R.). R.A.C. is a Wellcome Senior Investigator (103895/Z/14/Z).

1. Cross RA, McAinsh A (2014) Prime movers: The mechanochemistry of mitotic kinesins. *Nat Rev Mol Cell Biol* 15(4):257–271.
2. Kashina AS, et al. (1996) A bipolar kinesin. *Nature* 379(6562):270–272.
3. Tao L, et al. (2006) A homotetrameric kinesin-5, KLP61F, bundles microtubules and antagonizes Ncd in motility assays. *Curr Biol* 16(23):2293–2302.
4. Yildiz A, Tomishige M, Gennerich A, Vale RD (2008) Intramolecular strain coordinates kinesin stepping behavior along microtubules. *Cell* 134(6):1030–1041.
5. Kapitein LC, et al. (2008) Microtubule cross-linking triggers the directional motility of kinesin-5. *J Cell Biol* 182(3):421–428.
6. van den Wildenberg SM, et al. (2008) The homotetrameric kinesin-5 KLP61F preferentially crosslinks microtubules into antiparallel orientations. *Curr Biol* 18(23):1860–1864.
7. Kapitein LC, et al. (2005) The bipolar mitotic kinesin Eg5 moves on both microtubules that it crosslinks. *Nature* 435(7038):114–118.
8. Weinger JS, Qiu M, Yang G, Kapoor TM (2011) A nonmotor microtubule binding site in kinesin-5 is required for filament crosslinking and sliding. *Curr Biol* 21(2):154–160.
9. Roostalu J, et al. (2011) Directional switching of the kinesin Cin8 through motor coupling. *Science* 332(6025):94–99.
10. Avunie-Masala R, et al. (2011) Phospho-regulation of kinesin-5 during anaphase spindle elongation. *J Cell Sci* 124(Pt 6):873–878.
11. Hildebrandt ER, Gheber L, Kingsbury T, Hoyt MA (2006) Homotetrameric form of Cin8p, a *Saccharomyces cerevisiae* kinesin-5 motor, is essential for its in vivo function. *J Biol Chem* 281(36):26004–26013.
12. Thiede C, Lakämper S, Wessel AD, Kramer S, Schmidt CF (2013) A chimeric kinesin-1 head/kinesin-5 tail motor switches between diffusive and processive motility. *Biophys J* 104(2):432–441.
13. Fakhri N, et al. (2014) High-resolution mapping of intracellular fluctuations using carbon nanotubes. *Science* 344(6187):1031–1035.
14. Scholey JE, Nithianantham S, Scholey JM, Al-Bassam J (2014) Structural basis for the assembly of the mitotic motor kinesin-5 into bipolar tetramers. *eLife* 3:e02217.
15. Gerson-Gurwitz A, et al. (2011) Directionality of individual kinesin-5 Cin8 motors is modulated by loop 8, ionic strength and microtubule geometry. *EMBO J* 30(24):4942–4954.

16. Shapira O, Gheber L (2016) Motile properties of the bi-directional kinesin-5 Cin8 are affected by phosphorylation in its motor domain. *Sci Rep* 6:25597.
17. Düselder A, et al. (2015) Deletion of the tail domain of the kinesin-5 Cin8 affects its directionality. *J Biol Chem* 290(27):16841–16850.
18. Fridman V, et al. (2013) Kinesin-5 Kip1 is a bi-directional motor that stabilizes microtubules and tracks their plus-ends in vivo. *J Cell Sci* 126(Pt 18):4147–4159.
19. Edamatsu M (2014) Bidirectional motility of the fission yeast kinesin-5, Cut7. *Biochem Biophys Res Commun* 446(1):231–234.
20. Akera T, Goto Y, Sato M, Yamamoto M, Watanabe Y (2015) Mad1 promotes chromosome congression by anchoring a kinesin motor to the kinetochore. *Nat Cell Biol* 17(9):1124–1133.
21. Waitzman JS, Rice SE (2014) Mechanism and regulation of kinesin-5, an essential motor for the mitotic spindle. *Biol Cell* 106(1):1–12.
22. Thiede C, Fridman V, Gerson-Gurwitz A, Gheber L, Schmidt CF (2012) Regulation of bidirectional movement of single kinesin-5 Cin8 molecules. *BioArchitecture* 2(2):70–74.
23. Crevel IM, Lockhart A, Cross RA (1996) Weak and strong states of kinesin and ncd. *J Mol Biol* 257(1):66–76.
24. Stock MF, Chu J, Hackney DD (2003) The kinesin family member BimC contains a second microtubule binding region attached to the N terminus of the motor domain. *J Biol Chem* 278(52):52315–52322.
25. Goulet A, et al. (2012) The structural basis of force generation by the mitotic motor kinesin-5. *J Biol Chem* 287(53):44654–44666.
26. Parke CL, Wojcik EJ, Kim S, Worthylake DK (2010) ATP hydrolysis in Eg5 kinesin involves a catalytic two-water mechanism. *J Biol Chem* 285(8):5859–5867.
27. Hwang W, Lang MJ, Karplus M (2008) Force generation in kinesin hinges on cover-neck bundle formation. *Structure* 16(1):62–71.
28. Carter AP, et al. (2008) Structure and functional role of dynein's microtubule-binding domain. *Science* 322(5908):1691–1695.
29. Leduc C, et al. (2012) Molecular crowding creates traffic jams of kinesin motors on microtubules. *Proc Natl Acad Sci USA* 109(16):6100–6105.
30. Shimamoto Y, Forth S, Kapoor TM (2015) Measuring pushing and braking forces generated by ensembles of kinesin-5 crosslinking two microtubules. *Dev Cell* 34(6):669–681.
31. Kaseda K, Crevel I, Hirose K, Cross RA (2008) Single-headed mode of kinesin-5. *EMBO Rep* 9(8):761–765.
32. Sindelar CV, Downing KH (2007) The beginning of kinesin's force-generating cycle visualized at 9-A resolution. *J Cell Biol* 177(3):377–385.
33. Braun M, Drummond DR, Cross RA, McAinsh AD (2009) The kinesin-14 Klp2 organizes microtubules into parallel bundles by an ATP-dependent sorting mechanism. *Nat Cell Biol* 11(6):724–730.
34. Sindelar CV, Downing KH (2010) An atomic-level mechanism for activation of the kinesin molecular motors. *Proc Natl Acad Sci USA* 107(9):4111–4116.
35. Ludtke SJ, Baldwin PR, Chiu W (1999) EMAN: Semiautomated software for high-resolution single-particle reconstructions. *J Struct Biol* 128(1):82–97.
36. Frank J, et al. (1996) SPIDER and WEB: processing and visualization of images in 3D electron microscopy and related fields. *J Struct Biol* 116(1):190–199.
37. Grigorieff N (2007) FREALIGN: High-resolution refinement of single particle structures. *J Struct Biol* 157(1):117–125.
38. Pettersen EF, et al. (2004) UCSF Chimera–a visualization system for exploratory research and analysis. *J Comput Chem* 25(13):1605–1612.
39. Pandurangan AP, Topf M (2012) Finding rigid bodies in protein structures: Application to flexible fitting into cryoEM maps. *J Struct Biol* 177(2):520–531.